Increasing impact ionization rates in Si nanoparticles through surface engineering: A density functional study

Márton Vörös, Dario Rocca, Giulia Galli, Gergely T. Zimanyi, and Adam Gali

Phys. Rev. B **87**, 155402 — Published 4 April 2013

DOI: 10.1103/PhysRevB.87.155402

Increasing impact ionization rates in Si nanoparticles through surface engineering: a density functional study

Márton Vörös,[1] Dario Rocca,[2] Giulia Galli,[2,3] Gergely T. Zimanyi,[3] and Adam Gali[1,4]

[1] *Department of Atomic Physics, Budapest University of Technology and Economics, Budafoki út 8., H-1111, Budapest, Hungary*
[2] *Chemistry Department, University of California, Davis, California 95616, USA*
[3] *Physics Department, University of California, Davis, California 95616, USA*
[4] *Institute for Solid State Physics and Optics, Wigner Research Center for Physics, Hungarian Academy of Sciences, P.O. Box 49, H-1525 Budapest*

We propose design pathways to improve the efficiency of Multiple Exciton Generation (MEG) in nanoparticle-based solar cells by carrying out ab-initio calculations of impact ionization (II) rates in semiconducting nanoparticles (NPs). In NPs with unreconstructed surfaces, quantum confinement has two competing effects: it enhances the effective Coulomb interaction and thus the II rates, but it also blue-shifts the gap, which tends to reduce the II rates. The competition of these effects determines the utility of NP based solar cells. We report that surface reconstruction of NPs can tip the balance towards the enhancement of II by creating a substantial density of states at lower energies. Our results suggest that manipulating the surfaces of NPs, e.g. by engineering the ligands and embedding structures, may lead to an efficient multi-exciton generation within the solar spectrum.

PACS numbers: 78.67.Bf, 73.22.-f, 71.15.Qe, 88.40.-j

I. INTRODUCTION

In first and second generation solar cells most photo-excited electrons relax by emitting phonons, misdirecting a large portion of the absorbed solar energy into the vibrational channel[1]. One of the focus of third generation photovoltaics[2] is to retain a larger portion of the absorbed energy in the electronic sector. The Multiple Exciton Generation (MEG) paradigm is one of the most promising third generation photo-voltaic (PV) proposal to achieve this goal in which the photo-excited electrons relax by exciting additional excitons instead of phonons.

While in semiconducting bulk materials the efficiency of MEG was shown to be disappointingly low[3], Nozik proposed[4,5] that in nanoparticles (NPs) MEG may be faster than the phonon relaxation, making NP-based solar cells a viable candidate to enhance the efficiency of solar energy conversion. Motivated by this proposal, the presence of MEG was indeed demonstrated experimentally in several different semiconductor nanocrystals[6–9] including colloidal silicon NPs[10] and Si NPs embedded in a SiO_2 matrix[11,12]. While the efficiency of MEG in nanoparticles became the subject of debate[3,13–16], recently[17,18] a consensus emerged that MEG is indeed capable of generating up to 2.5 electrons per incoming photon in colloidal NPs[17,19–21], albeit at higher energies than initially reported. Finally, a remarkable paper reported very recently the first successful extraction of the multiple excitons from PbSe NPs to the charge transport layers of a functioning solar cell with an external quantum efficiency of 120%[22]. An analogous work also reported harnessing MEG in a PbS_xSe_{1-x} NP solar cell with favorable synthesis methods[23].

The theoretical understanding of MEG in NP solar cells soon focused on the primary role of quantum confinement enhancing the Coulomb interaction[6,24]. Three proposals were put forward to capture the physics of MEG: impact ionization (II)[25], virtual exciton generation[26], and evolution of coherent exciton states[27]. Starting with a general Hamiltonian[28], Piryatinski and Velizhanin analyzed the relative importance of these channels and argued that the impact ionization channel is the dominant process in PbSe[29]. An alternative unifying picture using a Green's function formalism was suggested by Baer and Rabani[30].

Other theoretical approaches, based on simplified empirical models[25], pointed out that while the quantum confinement of the electrons in the NPs enhances the Coulomb interaction and thus MEG, it also blue-shifts the effective band gap to higher values and thus decreases the electronic density of states (EDOS) in the low energy region of the conduction band that falls within the solar spectrum. This effect may reduce the utility of MEG for solar applications.[3,31] Stated otherwise, quantum confinement enhances MEG on relative energy scales, the energy being measured in the units of the NP band gap, while it reduces MEG on absolute energy scales[17,18].

In this paper we show that by appropriately engineering surface reconstructions of semiconducting nanoparticles the EDOS at low energy is increased which translates to an increased MEG efficiency on absolute energy scales. Our work focused on Si NPs because Si is environmentally friendly and Earth abundant. In spite of these positives, exploration of MEG in Si NPs has barely begun[11,12,31].

In particular, we report the study of bi-exciton generation in Si nanoparticles of diameter up to 2 nm, within the framework of Density Functional Theory (DFT), with the dielectric matrix obtained within the Random Phase Approximation (RPA) and by taking into account the probability of the formation of the initial exciton, therefore only bright excitons are included in our formalism. We found that (i) the impact ionization rate of smaller NPs outperformed larger ones' on relative energy scales; (ii) it was possible to preserve this increased MEG efficiency even on absolute energy scales by engineering surface reconstructions that increased the EDOS at low energy; (iii) the Coulomb interaction exhibited an unexpectedly strong energy dependence, changing by more than an order of magnitude in the energy range of interest of $2\times E_g$ to $3\times E_g$, E_g being the gap of the NPs; (iv) the electrons contribute more to the impact ionization rate than the holes in larger NPs; (v) the generation of bi-excitons via impact ionization was at least two orders of magnitude faster than their recombination by Auger decay.

The rest of the paper is organized as follows: in Section II we describe our theoretical and computational approach; in Section III we report our results, followed by our conclusions in Section IV.

II. METHODOLOGY

Fig. 1 depicts the formation of multiple excitons in the the two-step process considered in our study: first a single exciton is excited by a photon, then this exciton decays to multiple excitons via coulomb scattering; the (a)→(b) process is taken into account by calculating the oscillator strength of the transition, while the (b)→(c) transition is calculated in the impact ionization framework.

A. Calculation of impact ionization rates

We used the Fermi's golden rule to calculate the decay rate of excitons to bi-excitons:

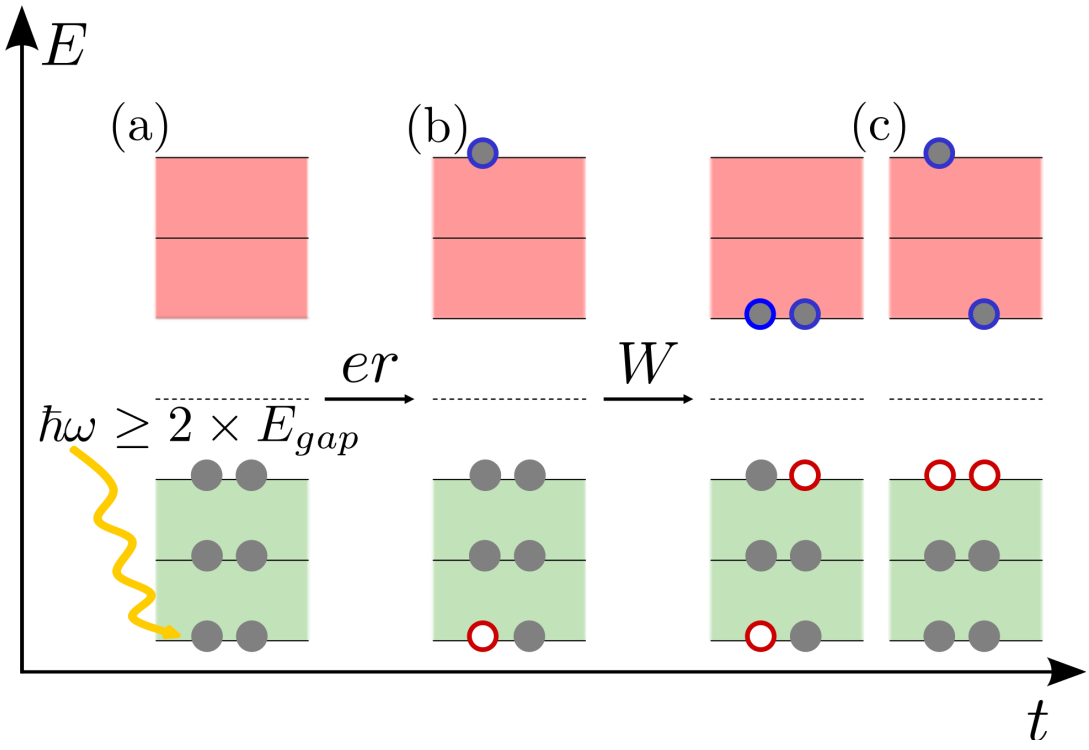

FIG. 1. Schematic representation of an impact ionization process. (a) If a photon with energy ($\hbar\omega$) two times larger than the band gap (E_{gap}) is absorbed (b) then the generated hot carriers may decay to (c) bi-excitons by exciting an additional electron-hole pair via Coulomb scattering. The physical interactions involved in the processes are also depicted: dipole (er) for the absorption process and screened Coulomb interaction (W) for impact ionization.

$$\Gamma_i^{\mathrm{II}} = \frac{2\pi}{\hbar}\sum_f |\langle X_i|W|XX_f\rangle|^2\delta(E_i - E_f), \tag{1}$$

where the initial exciton (X_i) and final bi-exciton states (XX_f) are approximated as singly and doubly excited Slater-determinants built up from DFT orbitals: $|\mathrm{X}_{j\sigma}^{a\sigma}\rangle = a_{a\sigma}^\dagger a_{j\sigma}|\mathrm{GS}\rangle$, $|\mathrm{XX}_{k\sigma_3 l\sigma_4}^{b\sigma_1 c\sigma_2}\rangle = a_{b\sigma_1}^\dagger a_{c\sigma_2}^\dagger a_{k\sigma_3} a_{l\sigma_4}|\mathrm{GS}\rangle$. Here, GS is the ground state Slater-determinant, $a^\dagger$ and a are the creation and annihilation operators, respectively, while the indices a, b, c and j, k, l denote unoccupied and occupied states, respectively, with corresponding spin states σ. In Eq. 1 i is the cumulative notation for the indices a, j, σ and f for the indices $b, c, k, l, \sigma_1, \sigma_2, \sigma_3, \sigma_4$. The energies of the initial and final states are $E_i = \epsilon_a - \epsilon_j$, $E_f = \epsilon_b - \epsilon_l + \epsilon_c - \epsilon_k$ and W stands for the screened Coulomb interaction. After carrying out the summations, and omitting the spin index of the initial state, the impact ionization (or transition) rates are given as a sum of two contributions ($\Gamma_{ja}^{\mathrm{II}} = \Gamma_j^{\mathrm{II}+} + \Gamma_a^{\mathrm{II}-}$):

$$\begin{aligned}\Gamma_j^{\mathrm{II}+} &= 2\frac{2\pi}{\hbar}\sum_{klc}(|V_{lckj} - V_{kclj}|^2 + |V_{lckj}|^2 + |V_{kclj}|^2) \\ &\quad\times\delta[\epsilon_j - (\epsilon_l - \epsilon_c + \epsilon_k)] \qquad (2a)\\ \Gamma_a^{\mathrm{II}-} &= 2\frac{2\pi}{\hbar}\sum_{lbc}(|V_{aclb} - V_{ablc}|^2 + |V_{aclb}|^2 + |V_{ablc}|^2) \\ &\quad\times\delta[\epsilon_a - (\epsilon_b - \epsilon_l + \epsilon_c)] \qquad (2b)\end{aligned}$$

Here V_{rsut} is the six dimensional Coulomb integral: $V_{rsut} = \int\int d^3r d^3r' \psi_r^*(\mathbf{r})\psi_s(\mathbf{r})W(\mathbf{r},\mathbf{r}')\psi_u^*(\mathbf{r}')\psi_t(\mathbf{r}')$, where the screened Coulomb interaction $W(\mathbf{r},\mathbf{r}')$ is calculated within the static RPA: $W(\mathbf{r},\mathbf{r}') = \int d^3r'' \epsilon_{\mathrm{RPA}}^{-1}(\mathbf{r},\mathbf{r}'')\frac{e^2}{4\pi\epsilon_0|\mathbf{r}'-\mathbf{r}''|}$, where $\epsilon_{\mathrm{RPA}}(\mathbf{r},\mathbf{r}') = \delta(\mathbf{r}-\mathbf{r}'') - \int d^3r'' v(\mathbf{r},\mathbf{r}'')\chi(\mathbf{r}'',\mathbf{r}')$, χ is the static Kohn-Sham independent particle polarizability, and v is the bare Coulomb potential.

The two terms of Eq. 2 represent two distinct relaxation channels: the term with index j represents the case when positively charged holes relax to positive trions, while the term with index a corresponds to the channel when negatively charged electrons relax to negative trions, where trions are a combination of a single particle and an electron-hole pair.

To analyze the results of our calculations, we introduce the single-particle trion density of states, $TDOS_i$, at energy ϵ_i, which is calculated by summing all Dirac deltas of Eq. 2: eg. the positive trion density of states is given by $TDOS_i = \sum_{klc} \delta[\epsilon_i - (\epsilon_l - \epsilon_c + \epsilon_k)]$. In the same vein, the single-particle effective Coulomb matrix element, or Coulomb interaction, at energy ϵ_i, W^i_{eff}, was calculated by isolating $TDOS_i$ within the impact ionization rate $\Gamma^{\rm II}_i$, both evaluated at the energy ϵ_i: $\Gamma^{\rm II}_i = \frac{2\pi}{\hbar}|W^i_{eff}|^2 TDOS_i$, where i represented either an electron or a hole.

The single-particle-averaged impact ionization rate of a photo-generated high energy exciton of energy E into a bi-exciton was obtained by summing all the single-particle exciton impact ionization rates $\Gamma^{\rm II}_{ja}$ for which the energy difference of the constituent single-particle states equaled E: $\epsilon_a - \epsilon_j = E$, properly normalizing the sum with the number of single-particle states:

$$\overline{\Gamma}^{\rm II}(E) = \frac{\sum_{ja} \Gamma^{\rm II}_{ja} f_{ja} \delta[(\epsilon_a - \epsilon_j) - E]}{\sum_{ja} f_{ja} \delta[(\epsilon_a - \epsilon_j) - E]} \tag{3}$$

Here $f_{ja} = \frac{1}{3}\sum_{r'=x,y,z} |\int \psi^*_j(\mathbf{r}) r' \psi_a(\mathbf{r}) d^3r|^2$ is the direction averaged squared transition dipole. By including this factor as a weight in the single-particle-averaged rate, we take into account the fact that only bright excitons can decay into bi-excitons, i.e. those, whose oscillator strength is larger than zero (see Appendix A).

The energy levels in Eqs. 2-3 were broadened with a width Δ to accommodate energy conservation. Energy summations were properly normalized and the independence of our results from Δ has been extensively verified in the energy range of interest (details are reported in Appendix B).

Importantly, Eq. 3 inherently includes all the key factors that determine the final impact ionization rate: (i) how much the effective Coulomb interaction W_{eff} is enhanced in NPs, (ii) whether the $GS \rightarrow X$ transition is allowed, and (iii) how large is the density of final states.

The calculation of impact ionization rates was implemented as a post-processing module of the QUANTUM-ESPRESSO[32] DFT code, which uses pseudopotentials and plane waves as a basis set. We used the PBE approximation[33] to describe the exchange correlation functional entering the KS Hamiltonian and norm-conserving pseudopotentials[34], with a cutoff of 25 Ry to compute the single particle wavefunctions. The inverse dielectric matrix entering the calculation of the screened single particle Coulomb matrix element W was obtained using the spectral decomposition technique proposed in Refs. 35–37: $\epsilon^{-1}_{\rm RPA} = 1 + \sum_i^M |\phi_i\rangle(\lambda_i^{-1} - 1)\langle\phi_i|$, where ϕ_i is the ith eigenpotential of the static dielectric function with eigenvalue λ_i. We found that for the system considered here, with up to 1024 electrons, M=800 is sufficient to obtain a well converged $\epsilon^{-1}_{\rm RPA}$.

B. Structural models of Si nanoparticles

Nanoparticle geometries were generated by cutting out spherical nanoparticles from bulk silicon supercells in such a way that at most two dangling bonds per surface atom are formed, dangling bonds were passivated by hydrogen atoms. We considered the following nanoparticles: $Si_{35}H_{36}$, $Si_{66}H_{64}$, $Si_{78}H_{64}$, $Si_{124}H_{96}$, $Si_{220}H_{144}$. Our largest nanocrystal reaches the experimental size of ≈2.0 nm in diameter. The diameter is defined as the maximum distance between Si-Si atoms; our structural models are shown in Fig. 2. The average core Si-Si bond length is 2.32 Å and the average Si-H bond length is 1.52 Å. Minimization of the total energy with respect to the position of the nuclei was carried out with the stringent criteria on the forces of 10^{-5}Ry/Bohr and a 35Ry planewave cutoff. In order to minimize the interaction of nanoparticles with periodic images from neighboring cells, we employed a 10Å vacuum separation. To investigate the effect of surface reconstruction, we removed some selected hydrogen atoms, and then determined the closest total energy minimum. We found that long Si-Si surface bonds with a bond length of ≈ 2.46Å formed on the surface of $Si_{66}H_{40}$ and $Si_{220}H_{120}$. See Fig. 2 for the geometries of all the NPs considered in our study. This atomic rearrangement closely resembles the usual 2×1 surface reconstruction of (100) Si surfaces. We note that Si NPs with reconstructed surfaces were predicted to be more stable than Si NPs without reconstruction, under certain experimental preparation conditions (e.g. the chemical potential of hydrogen)[38–40]. Recent measurements indicated that such reconstructed nanoparticles might indeed form[41].

We report the diameter and Kohn-Sham gap of considered NPs in Table I. We note that DFT gaps tend to be lower estimates of true quasiparticle gaps but the inclusion excitonic interaction seems to cancel quasiparticle effects, at least for silicon NPs[42].

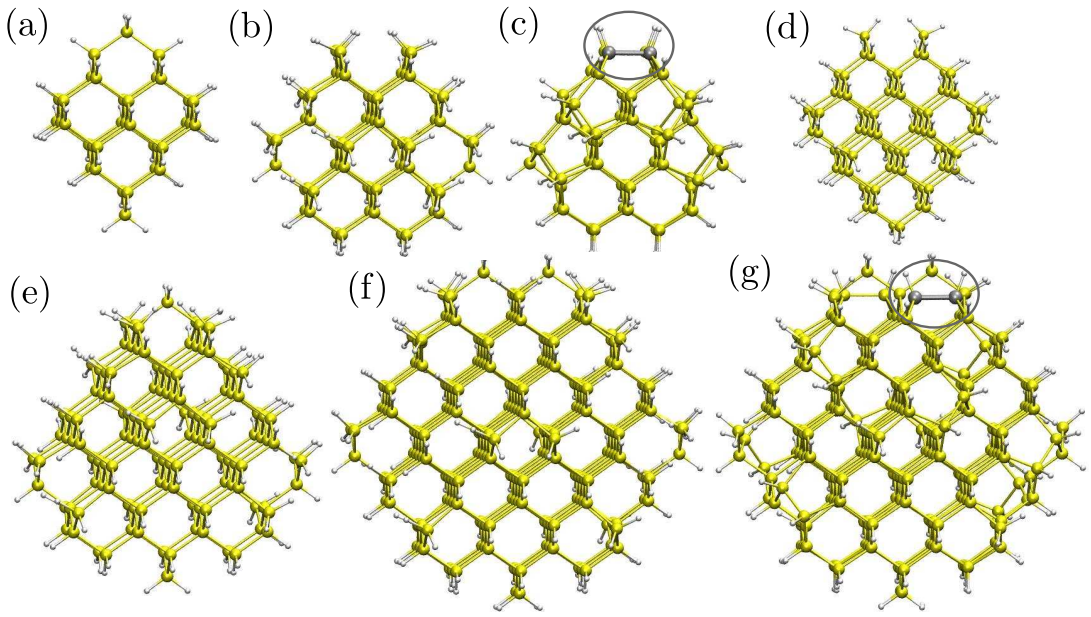

FIG. 2. Ball-and-stick geometries of the nanoparticles considered in our work. NP with non-reconstructed surfaces: (a) $Si_{35}H_{36}$, (b) $Si_{66}H_{64}$, (d) $Si_{78}H_{64}$, (e) $Si_{124}H_{96}$, (f) $Si_{220}H_{144}$, and with reconstructed ones: (c) $Si_{66}H_{40}$, and (g) $Si_{220}H_{120}$. Representative long Si-Si bonds arising from surface reconstruction are shown in grey. Yellow (white) spheres represent silicon (hydrogen) atoms.

TABLE I. The atomic structure of the studied NPs and their calculated gap. First, second, third and fourth columns: formula, type of reconstruction, diameter and Kohn-Sham gaps, respectively.

Formula	Rec	d (nm)	gap (eV)
$Si_{35}H_{36}$	No	1.1	3.5
$Si_{66}H_{64}$	No	1.2	2.9
$Si_{66}H_{40}$	2×1	1.2	1.94
$Si_{78}H_{64}$	No	1.4	2.75
$Si_{124}H_{96}$	No	1.6	2.37
$Si_{220}H_{144}$	No	2	2.0
$Si_{220}H_{120}$	2×1	2	2.0

III. RESULTS AND DISCUSSION

We first analyzed the effects of quantum confinement as a function of the nanoparticle size. When the impact ionization is plotted against the commonly used relative energy scale (that is, energy renormalized by the gap of the NP), we found that smaller nanoparticles have higher rates than larger ones [Fig. 3(a)]. On the other hand, with decreasing NP diameter the electronic band gap is increased, reducing the EDOS at low energies thus pushing the threshold of the activation of impact ionization to higher energies on absolute energy scales [see Fig. 3(b)]. These findings confirm previous tight-binding[43] and pseudopotential[44] calculations.

In sum, Fig. 3 shows that for non-reconstructed NPs, on absolute energy scales the EDOS reduction prevailed over the interaction enhancement, leading to a reduction of the impact ionization rate $\overline{\Gamma}$.

In the following we describe strategies that can compensate the electronic gap increase due to quantum confinement. One way to decrease the gap of small NPs and increase their EDOS at low energies is to reconstruct their surfaces[38–40,45]. Thus, we investigated the effect of surface reconstruction on the impact ionization (II) rates by comparing results obtained for 1.2 and 2.0 nm NPs with and without reconstructed surfaces.

We explored the best-known, (2×1)-type of surface reconstruction for Si. For a d=1.2 nm NP, this reconstruction gave rise to a class of low energy states, reducing the gap by 1 eV and enhancing the impact ionization rate [Fig. 4(a)].

For the 2 nm NP the gap was not reduced by the reconstruction [Table I]. Since the total impact ionization rate is the product of the effective matrix element W_{eff} and TDOS we analyzed these contributions separately to understand the origin of the increased impact ionization rate. While the TDOS for the reconstructed nanoparticle was on average

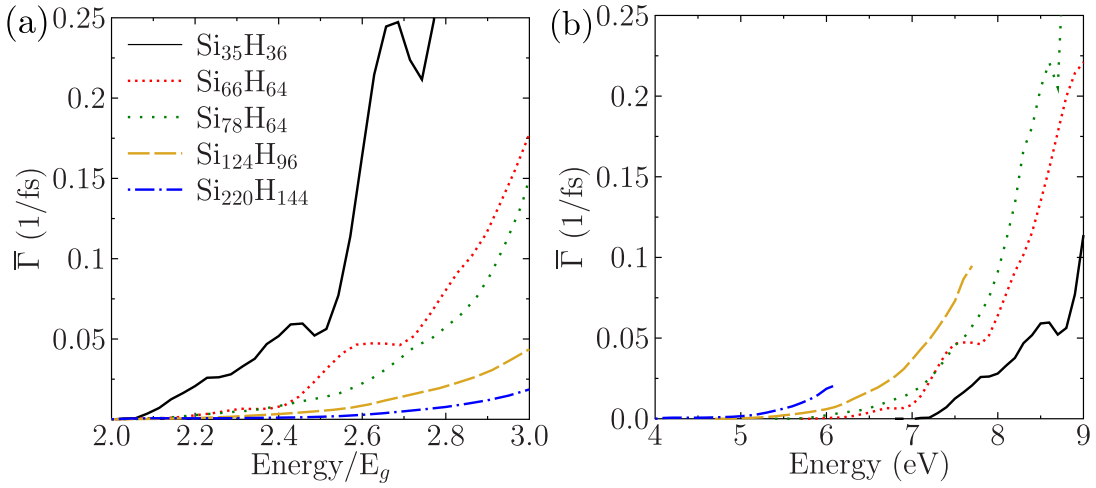

FIG. 3. Size dependence of the single-particle-averaged impact ionization rate for non-reconstructed clusters: (a) rate plotted on an absolute energy scale; (b) rate plotted on a relative energy scale, the energy being normalized with the gap of the corresponding nanoparticle. The color code for the lines in (b) is the same as in (a). Note that while in (a) the largest d=2.0 nm nanoparticle has the highest impact ionization rate, the opposite is true in (b) where the smallest d=1.1 nm nanoparticle wins.

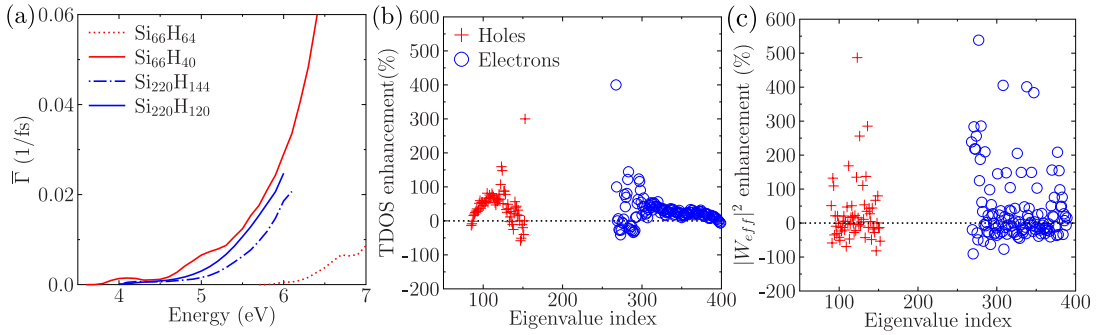

FIG. 4. (a) Impact ionization rate for the d=1.2 nm and d=2.0 nm nanoparticle with and without surface reconstruction. (b) Enhancement of the electron and hole trion density of states (TDOS) due to surface reconstruction for the d=2 nm nanoparticle. (c) Enhancement of the effective matrix element (W_{eff}, see text) due to surface reconstruction for the d=2 nm nanoparticle. The color code for the markers in (c) is the same as in (b).

larger than that of the non-reconstructed one [Fig. 4(b)], the enhancement of the effective matrix element was closer to zero [Fig. 4(c)], shown separately for holes and electrons.

Comparing the II rates for the two NP sizes reveals that the reduction of the EDOS by quantum confinement in the smaller NPs can be more than compensated by the enhancement of the interactions when the surface reconstruction is taken into account. In fact, surface reconstruction can lead to a a promising overall 20-30% increase of the II rate in the energy range of interest. These observations offer a mechanism to resolve the competing effects of quantum confinement and to harness the promise of MEG for solar energy conversion.

To gain a more detailed picture of the II process, we separately analyzed the contribution of holes and electrons to the computed II rates (Eq. 2). As shown in Fig. 5(a), the single-particle-averaged ionization rate of hole-mediated processes showed an oscillatory behavior in the 1.1 nm nanoparticle. These oscillations were driven by the density of the valence band EDOS being less than that of the conduction band, as well as the higher single particle rates for holes than for electrons. Surprisingly, the TDOS was in general larger for electrons; hence one expected W_{eff} to be smaller for electrons than for holes, and indeed this was found to be the case (Fig. 5(b)).

To investigate the origin of this difference between electrons and holes, we computed the inverse participation ratio (IPR): $\frac{\int |\psi_i(\mathbf{r})|^4 d^3r}{(\int |\psi_i(\mathbf{r})|^2 d^3r)^2}$. The larger the IPR, the higher the degree of localization. We found that the IPR for the hole states was substantially larger than for the active electron states, i.e. those electronic states with energy large enough to contribute to the bi-exciton generation (Fig. 5(b)).

As the NP size increased, the asymmetry between holes and electrons is expected to tend toward its bulk value.

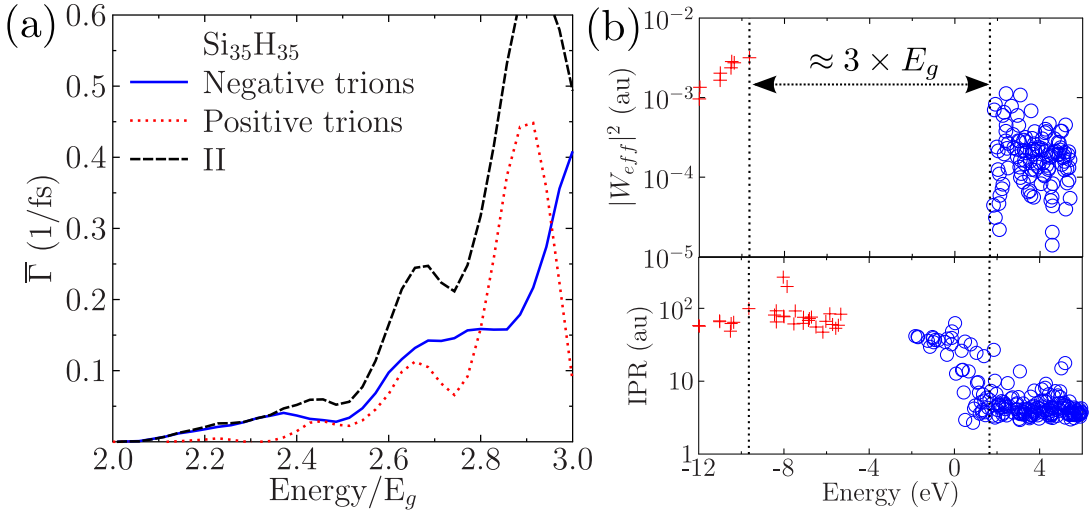

FIG. 5. (a) Hole and electron contributions (Eq. 2) to the averaged II rate for the d=1.1 nm nanoparticle. Blue solid and red dotted lines represent electron and hole impact ionization rates, respectively. (b) Comparison of the effective matrix element and inverse participation ratio for the same nanoparticle. Blue crosses, red circles denote electron and hole quantities. Double headed arrows show a gap of approximately $3 \times E_g$ in W_{eff}, IPR.

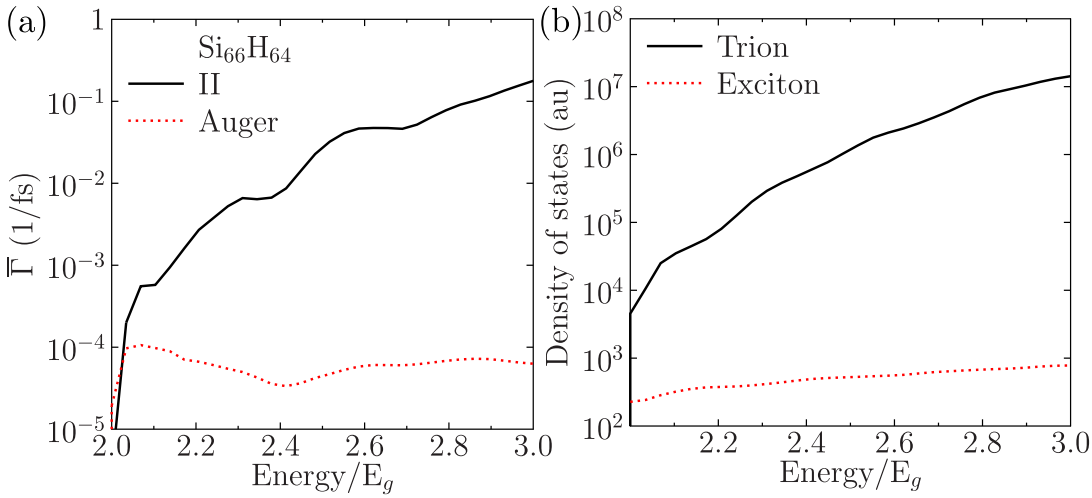

FIG. 6. (a) Averaged impact ionization and Auger recombination rate for the d=1.2 nm nanoparticle plotted on a relative energy scale. (b) Comparison of the number of exciton and bi-excitons corresponding to a given photon energy.

Since the degree of delocalization of holes and electrons is essentially the same in the bulk, we observed no asymmetry in the TDOS, W_{eff} and IPR, as expected. This however does not translate to a nearly equal contribution of electrons and holes to the single-particle-averaged II rate for the case of the 2 nm NP. The reason is that there are more holes than electrons that participate in building up *dark* excitons. As a consequence, the contribution of electrons is larger than that of the holes (details are given in Appendix C). The strong energy dependence of the effective matrix element (W_{eff}) has been recently observed by using atomistic pseudopotential calculations on a different material, CdSe nanoparticles with larger diameters than considered in our study[46].

The gains of the MEG processes could be used to boost the efficiency of solar energy conversion only if the generated bi-excitons could be extracted before they recombined into single excitons. To evaluate the competition of these time scales, we compared the rates of the Auger process, the primary recombination channel of the bi-excitons to those of the II process itself. The former may be computed by using the same matrix elements $| < X_i|W|XX_f > |^2$, obtained when computing the II rates, but in this case the final states are the single exciton states and the initial states are the bi-exciton states.

Fig. 6(a) shows that the bi-exciton generation rate was at least two orders of magnitude faster than the inverse Auger recombination process in most of the energy range of interest. A primary cause of this difference was that in

the impact ionization process the single particle states contributing to the bi-exciton final state can be combined in a much larger number of ways than the single particle states in the final states of the Auger process [cf. Fig. 6(b)]. This large difference between the ionization rate generating the bi-excitons and the Auger rate relaxing the bi-excitons, indicated that there existed a comfortable time window to extract bi-excitons, generated by the MEG process, before the constituent electrons and holes recombine. Our results are consistent with the findings reported in Ref. 25. They are also consistent with the experimentally observed bi-exciton generation rate being less than hundred of femtoseconds, and the bi-exciton Auger recombination rate being of the order of many tens or few hundreds of picoseconds[10,18].

IV. SUMMARY AND CONCLUSIONS

In summary, we computed impact ionization rates in silicon nanoparticles by using a fully ab-initio approach based on DFT, and with dielectric screening obtained from first principles employing spectral decomposition techniques. Our goal was to manage the two competing effects of quantum confinement on NPs: the enhancement of the Coulomb interaction that can increase MEG vs. the undesirable enlargement of the gap. We showed that the surface reconstruction of small Si nanoparticles may enhance the impact ionization rates compared to that of unreconstructed nanoparticles, while the Coulomb interaction remains enhanced with respect to that of the bulk, as in NP without reconstructed surfaces. We thus proposed that manipulating the surfaces of NPs by, e.g. engineering the type of chemisorbed ligands, or the interface between the NPs and their embedding matrices, one may enhance the multi-exciton generation within the solar spectrum. Our findings may allow the transfer of the gains of solar energy conversion promised by MEG from relative to absolute energy scales.

ACKNOWLEDGMENTS

The authors acknowledge support from NSF Solar Collaborative DMR-1035468. Work was also supported by Grant NSF CHE-0802907 and the National Development Agency, Hungary (TÁMOP - 4.2.2.B-10/1–2010-0009). MV wishes to thank Marco Govoni, Kirill Velizhanin, Stefan Wippermann, Zhibin Lin, Roi Baer, and Eran Rabani for useful discussions. GTZ thanks Bawendi, C. Delerue, V. Klimov, A. Nozik, and A. Zunger for valuable discussions.

Supercomputer access at the NIIF centre in Debrecen is gratefully acknowledged. Additional computational resources were provided by the NERSC high performance computing facility at LBL. This research also used ShaRCS, UC Shared Research Computing Services Cluster, which is technically supported by multiple UC IT divisions and managed by the University of California, Office of the President.

Appendix A: Effect of oscillator strengths

In Eq. 3 by setting all oscillator strengths (f_{ja}) to one, one obtains an arithmetic average of single particle transitions having energy E:

$$\overline{\Gamma}^{\mathrm{II}}(E) = \frac{\sum_{ja} \Gamma^{\mathrm{II}}_{ja} \delta[(\epsilon_a - \epsilon_j) - E]}{\sum_{ja} \delta[(\epsilon_a - \epsilon_j) - E]} \tag{A1}$$

Here we compare results obtained with and without including f_{ja}. Fig. 7 shows the comparison for non-reconstructed and reconstructed NPs. Generally it is found that in the energy range of interest, including oscillator strengths reduces the calculated impact ionization rates. This reduction is a clear consequence of the fact that some initial states (excitons) are dark – they cannot be excited via a photon –, thus their contribution to the final impact ionization rate is zero.

Fig. 8 shows the comparison of the contribution of electrons and holes to single-particle-averegad impact ionization rates for two selected NPs. The oscillatory behavior of the contribution of holes remains the same by performing an oscillator strength weighted average, as discussed in the paper (cf. Fig. 8(a) and (c)). However, for the larger NP there are more holes than electrons that participate in building up *dark* excitons. As a consequence, the contribution of electrons remains almost unchanged and the contribution of holes to averaged impact ionization rate is nearly halved (cf. Fig. 8(b) and (d)).

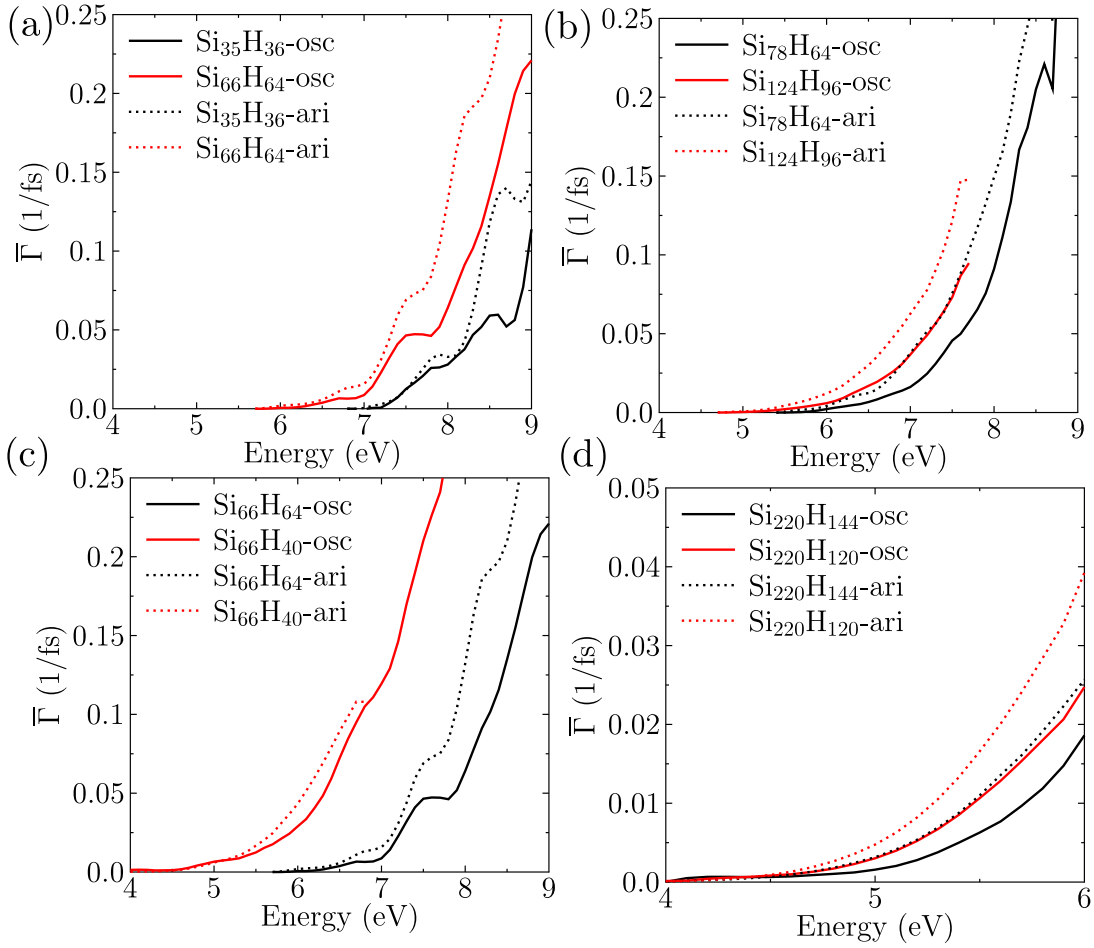

FIG. 7. Comparison of single-particle averaged impact ionization rates obtained with or without including oscillator strengths. (a) d=1.1 nm and d=1.2 nm NPs, (b) d=1.4 and d=1.6 nm NPs, (c) non-reconstructed ($Si_{66}H_{64}$) and reconstructed ($Si_{66}H_{40}$) d=1.2 nm NPs, (d) non-reconstructed ($Si_{220}H_{144}$) and reconstructed ($Si_{220}H_{120}$) d=2.0 nm NPs. Legends in the subfigures: "osc"/"ari" denote oscillator strength weighted/arithmetic average.

Appendix B: Dependence of the results on Δ

In our derivation, in Eq. 2, we used a window function centered at bare energies to represent the finite linewidth (Δ) of single particles. This smearing can be attributed for example to electron-phonon interaction effects, or to the coupling with the environment. In this case, the energy conservation rule becomes:

$$\delta(\epsilon) = \frac{\Theta(\epsilon + \frac{\Delta}{2}) - \Theta(\epsilon - \frac{\Delta}{2})}{\Delta}, \tag{B1}$$

where is $\Theta(\epsilon)$ is the step-function:

$$\Theta(\epsilon) = \begin{cases} 0 & \text{if } \epsilon < 0, \\ 1 & \text{if } \epsilon \geq 0. \end{cases} \tag{B2}$$

As can be seen in Fig. 9(a), for a 1.5 nm nanoparticle, variations as large as 10% can be observed, however the larger nanoparticle exhibits a lower degree of dependence on Δ. There are two competing factors; first as the smearing is decreased a smaller number of transitions is included in the summation of Eq. 2 of the manuscript, thus the overall rate decreases. Second, as the smearing is reduced the denominator decreases resulting in an increased quotient [Eq. B1]. These two factors tend to cancel each other in the energy range of interest, e.g. the energy scale defined by

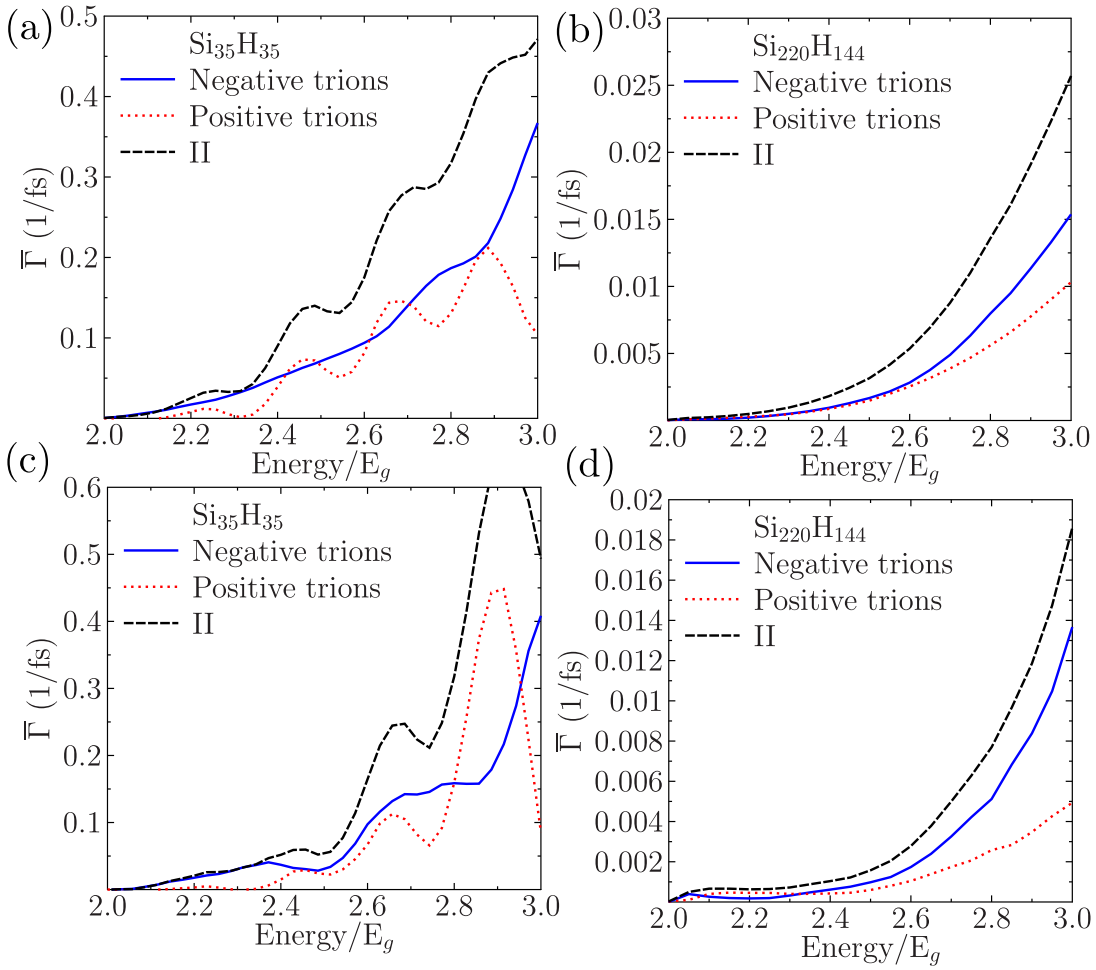

FIG. 8. Comparison of the contributon of electrons and holes to the single-particle averaged impact ionization rates obtained with or without including oscillator strengths. (a) d=1.1 nm NP without oscillator strength, (b) d=2.0 nm NP without oscillator strength, (c) d=1.1 nm NP with oscillator strength, (d) d=2.0 nm NP with oscillator strength.

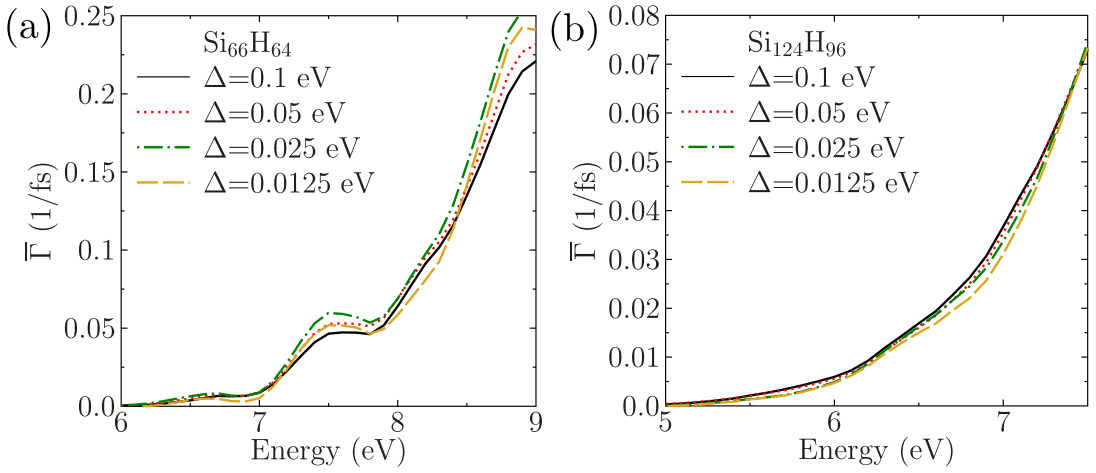

FIG. 9. Dependence of averaged impact ionization rates on the width of the window function (Δ) used to represent the energy conservation rule in Eq. 2: (a) d=1.2 nm NP (b) d=1.6 nm NP.

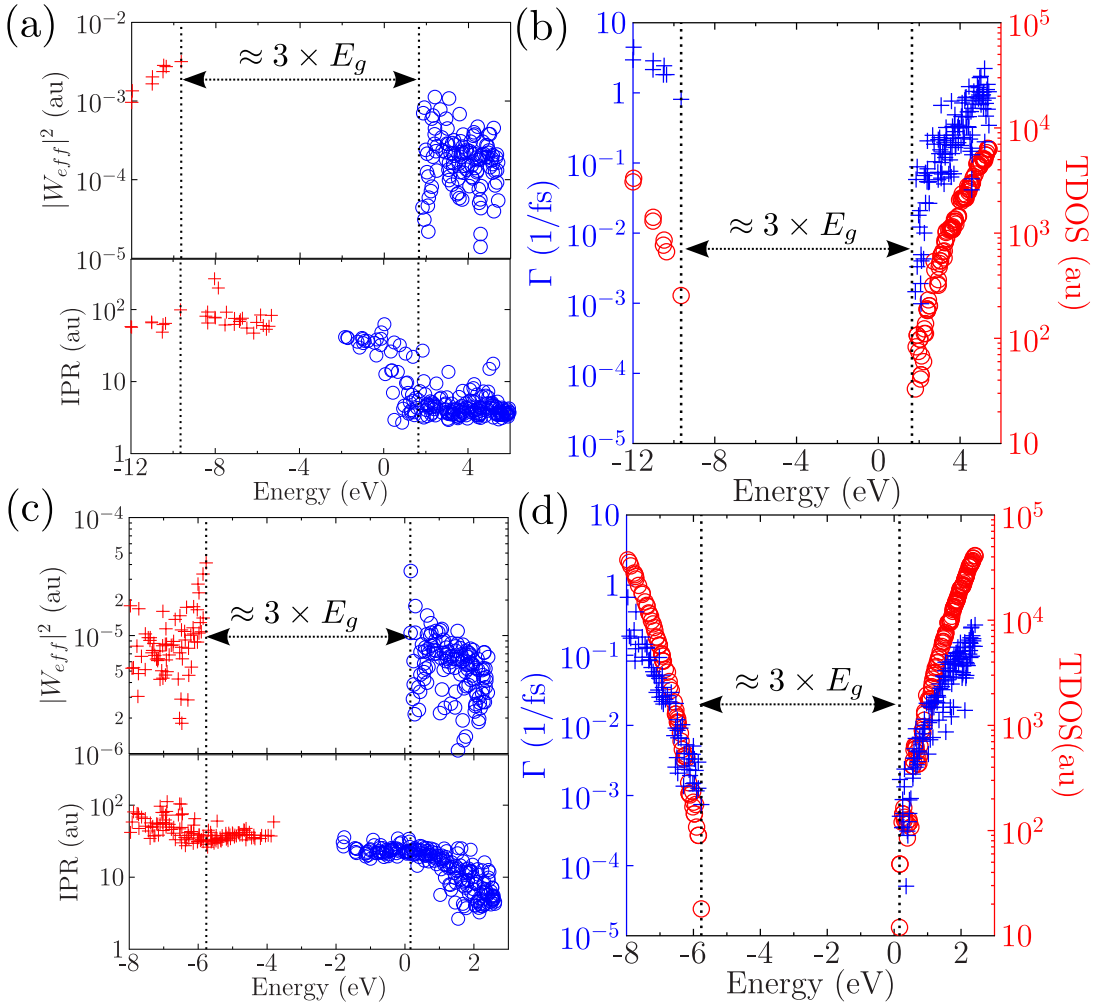

FIG. 10. (a) Comparison of the effective matrix element and inverse participation ratio for the d=1.1 nm nanoparticle. (b) Comparison of the single particle rate and trion density of states (TDOS) for the d=1.1 nm nanoparticle. (c),(d) subfigures show the same for the d=2 nm nanoparticle. Double headed arrows show a gap of approximately $3 \times E_g$ in Γ, W_{eff}, TDOS. For subfigures (a) and (c) blue crosses, red circles denote electron and hole quantities, while for subfigures (b) and (d) blue crosses, red circles represent Γ, TDOS, respectively.

room temperature is in the order of 0.02 eV. It is clear, that in the $\Delta \to 0$ limit, the impact ionization rate should converge to zero: there are only discrete electronic states in our treatment, thus it is very unlikely that the energy conservation rule of Eq. 2. would be satisfied.

Appendix C: Analysis of the contribution of holes and electrons

To gain a more detailed picture of the II process, we separately analyzed the contribution of holes and electrons to the computed II rates (Eq. 2). As shown in Fig. 5(a), the single-particle-averaged ionization rate of hole-mediated processes showed an oscillatory behavior in the d=1.1 nm nanoparticle. These oscillations were driven by the density of the valence band EDOS being less than that of the conduction band, as well as the higher single particle rates for holes than for electrons. The latter can be seen in Fig. 10(c) where single particle rates were plotted for the d=1.1 nm nanoparticle. Surprisingly, the TDOS was in general larger for electrons [Figure 10(c)]; hence one expected W_{eff} to be smaller for electrons than for holes, and indeed this was found to be the case, as shown in Figure 10(b).

As the NP size increased, the asymmetry between holes and electrons is expected to tend toward its bulk value. Since the degree of delocalization of holes and electrons is essentially the same in the bulk, with no asymmetry in the TDOS, W_{eff} and IPR. This however does not translate to a nearly equal contribution of electrons and holes to single-particle-averaged II rate for the case of the 2 nm NP. The reason is that there are more holes than electrons

that participate in building up *dark* excitons. As a consequence, the contribution of electrons is larger than that of the holes (cf. Fig. 5(b)).

We note that while quantities plotted against the photon energy started increasing at $2 \times E_g$ (see eg. Figs. 5(a),(b)), single particle transitions contributing to the impact ionization process (Γ, W_{eff}, TDOS) plotted against the single particle energy exhibited a gap of approximately $3 \times E_g$, where E_g was the gap of the NP (see Figs. 10(a),(b),(c),(d)). This was a consequence of energy conservation: holes close to the valence band maximum and electrons close to the conduction band minimum did not have enough energy to excite an additional electron-hole pair, thus they had infinite impact ionization lifetimes.

[1] W. Shockley and H. J. Queisser, Journal of Applied Physics **32**, 510 (1961).
[2] M. Green, *Third generation photovoltaics: advanced solar energy conversion*, Springer series in photonics (Springer, 2006).
[3] J. J. H. Pijpers, R. Ulbricht, K. J. Tielrooij, A. Osherov, Y. Golan, C. Delerue, G. Allan, and M. Bonn, Nature Physics **5**, 811 (2005).
[4] A. J. Nozik, Annual Review of Physical Chemistry **52**, 193 (2001).
[5] A. J. Nozik, Physica E: Low-dimensional Systems and Nanostructures **14**, 115 (2002).
[6] R. D. Schaller and V. I. Klimov, Physical Review Letters **92**, 186601 (2004).
[7] R. J. Ellingson, M. C. Beard, J. C. Johnson, P. Yu, O. I. Micic, A. J. Nozik, A. Shabaev, and A. L. Efros, Nano Letters **5**, 865 (2005).
[8] S. J. Kim, W. J. Kim, Y. Sahoo, A. N. Cartwright, and P. N. Prasad, Applied Physics Letters **92**, 031107 (2008).
[9] J. J. H. Pijpers, E. Hendry, M. T. W. Milder, R. Fanciulli, J. Savolainen, J. L. Herek, D. Vanmaekelbergh, S. Ruhman, D. Mocatta, D. Oron, A. Aharoni, U. Banin, and M. Bonn, The Journal of Physical Chemistry C **111**, 4146 (2007).
[10] M. C. Beard, K. P. Knutsen, P. Yu, J. M. Luther, Q. Song, W. K. Metzger, R. J. Ellingson, and A. J. Nozik, Nano Letters **7**, 2506 (2007).
[11] D. Timmerman, I. Izeddin, P. Stallinga, I. N. Yassievich, and T. Gregorkiewicz, Nature Photonics **2**, 105 (2008).
[12] D. Timmerman, J. Valenta, K. Dohnalova, W. D. A. M. de Boer, and T. Gregorkiewicz, Nature Nanotechnology **6**, 710 (2011).
[13] G. Nair and M. G. Bawendi, Physical Review B (Condensed Matter and Materials Physics) **76**, 081304 (2007).
[14] M. Ben-Lulu, D. Mocatta, M. Bonn, U. Banin, and S. Ruhman, Nano Letters **8**, 1207 (2008).
[15] M. T. Trinh, A. J. Houtepen, J. M. Schins, T. Hanrath, J. Piris, W. Knulst, A. P. L. M. Goossens, and L. D. A. Siebbeles, Nano Letters **8**, 1713 (2008).
[16] M. Ji, S. Park, S. T. Connor, T. Mokari, Y. Cui, and K. J. Gaffney, Nano Letters **9**, 1217 (2009).
[17] J. A. McGuire, M. Sykora, J. Joo, J. M. Pietryga, and V. I. Klimov, Nano Letters **10**, 2049 (2010).
[18] M. C. Beard, The Journal of Physical Chemistry Letters **2**, 1282 (2011).
[19] J. M. Luther, M. C. Beard, Q. Song, M. Law, R. J. Ellingson, and A. J. Nozik, Nano Letters **7**, 1779 (2007).
[20] G. I. Koleilat, L. Levina, H. Shukla, S. H. Myrskog, S. Hinds, A. G. Pattantyus-Abraham, and E. H. Sargent, ACS Nano **2**, 833 (2008).
[21] M. C. Beard, A. G. Midgett, M. Law, O. E. Semonin, R. J. Ellingson, and A. J. Nozik, Nano Letters **9**, 836 (2009).
[22] O. E. Semonin, J. M. Luther, S. Choi, H.-Y. Chen, J. Gao, A. J. Nozik, and M. C. Beard, Science **334**, 1530 (2011).
[23] G. Zhai, C. P. Church, A. J. Breeze, D. Zhang, G. B. Alers, and S. A. Carter, Nanotechnology **23**, 405401 (2012).
[24] A. J. Nozik, Inorganic Chemistry **44**, 6893 (2005).
[25] A. Franceschetti, J. M. An, and A. Zunger, Nano Letters **6**, 2191 (2006).
[26] R. D. Schaller, V. M. Agranovitch, and V. I. Klimov, Nature Physics **1**, 189 (2005).
[27] A. Shabaev, A. Efros, and A. Nozik, Nano Letters **6**, 2856 (2006).
[28] A. Piryatinski and K. A. Velizhanin, The Journal of Chemical Physics **133**, 084508 (2010).
[29] K. A. Velizhanin and A. Piryatinski, Phys. Rev. Lett. **106**, 207401 (2011).
[30] E. Rabani and R. Baer, Chemical Physics Letters **496**, 227 (2010).
[31] G. Allan and C. Delerue, Phys. Rev. B **77**, 125340 (2008).
[32] P. Giannozzi, S. Baroni, N. Bonini, M. Calandra, R. Car, C. Cavazzoni, D. Ceresoli, G. L. Chiarotti, M. Cococcioni, I. Dabo, A. D. Corso, S. de Gironcoli, S. Fabris, G. Fratesi, R. Gebauer, U. Gerstmann, C. Gougoussis, A. Kokalj, M. Lazzeri, L. Martin-Samos, N. Marzari, F. Mauri, R. Mazzarello, S. Paolini, A. Pasquarello, L. Paulatto, C. Sbraccia, S. Scandolo, G. Sclauzero, A. P. Seitsonen, A. Smogunov, P. Umari, and R. M. Wentzcovitch, J. Phys.: Condens. Matter **21**, 395502 (2009).
[33] J. P. Perdew, K. Burke, and M. Ernzerhof, Phys. Rev. Lett. **77**, 3865 (1996).
[34] We used the pseudopotentials Si.pbe-rrkj.UPF and H.pbe-vbc.UPF from www.quantum-espresso.org.
[35] H. F. Wilson, F. m. c. Gygi, and G. Galli, Phys. Rev. B **78**, 113303 (2008).
[36] H. F. Wilson, D. Lu, F. m. c. Gygi, and G. Galli, Phys. Rev. B **79**, 245106 (2009).
[37] H.-V. Nguyen and S. de Gironcoli, Phys. Rev. B **79**, 205114 (2009).
[38] A. Puzder, A. J. Williamson, F. A. Reboredo, and G. Galli, Phys. Rev. Lett. **91**, 157405 (2003).
[39] X. Yang, Y.-J. Zhao, H. Xu, and B. I. Yakobson, Phys. Rev. B **83**, 205314 (2011).
[40] X. Wang, R. Q. Zhang, S. T. Lee, T. Frauenheim, and T. A. Niehaus, Applied Physics Letters **93**, 243120 (2008).

[41] S. Rao, K. Mantey, J. Therrien, A. Smith, and M. Nayfeh, Phys. Rev. B **76**, 155316 (2007).
[42] C. Delerue, M. Lannoo, and G. Allan, Phys. Rev. Lett. **84**, 2457 (2000).
[43] G. Allan and C. Delerue, Phys. Rev. B **73**, 205423 (2006).
[44] A. Franceschetti, J. M. An, and A. Zunger, Nano Letters **6**, 2191 (2006).
[45] A. Gali, M. Vörös, D. Rocca, G. T. Zimanyi, and G. Galli, Nano Letters **9**, 3780 (2009).
[46] Z. Lin, A. Franceschetti, and M. T. Lusk, ACS Nano **5**, 2503 (2011).